Geoscience Data Journal

WILEY

Geoscience Data Journal | RMetS

DATA ARTICLE OPEN ACCESS

Fluorescence Quantum Efficiency Data for Europe 2018–2025

David Herrera[1] | Uwe Rascher[1,2] | Zbyněk Malenovský[3] | Bastian Siegmann[1]

[1]Forschungszentrum Jülich GmbH, Institute of Bio- and Geosciences, IBG-2: Plant Sciences, Jülich, Germany | [2]Faculty of Agricultural, Nutritional and Engineering Sciences, Institute of Crop Science and Resource Conservation, University of Bonn, Bonn, Germany | [3]Remote Sensing Research Group, Department of Geography, University of Bonn, Bonn, Germany

Correspondence: David Herrera (d.herrera@fz-juelich.de)

Received: 23 February 2026 | **Revised:** 23 February 2026 | **Accepted:** 7 March 2026

Keywords: drought | fluorescence quantum efficiency | SIF | TROPOMI

ABSTRACT

Top-of-canopy solar-induced chlorophyll fluorescence (SIF) is strongly affected by canopy structure and illumination conditions, which limits the use of current satellite-based SIF products for detecting vegetation stress. To address this, we present a new dataset that combines TROPOMI SIF observations with MODIS photosynthetically active radiation (PAR) data (MCD18C2/A2) to derive a fluorescence quantum efficiency (ΦF) product across continental Europe, the UK and Ireland and northern Africa from 2018 to 2025. The dataset has a spatial resolution of 0.05° and daily, decadal and monthly temporal coverage. Building on a multi-sensor ΦF formulation from the literature, a previous analysis in Germany demonstrated that ΦF is sensitive to agricultural drought, revealing stress-related signals with a two-day lag in both agricultural and forest ecosystems, signals that were not detectable using top-of-canopy SIF alone or traditional vegetation indices. The dataset includes all input bands, allowing users to adapt or refine the calculation of ΦF. It also provides quality layers, including phase angle, solar zenith angle (SZA), cloud fraction and the retrieval error of the top-of-canopy SIF product. This dataset is designed to facilitate further research on the relationship between ΦF and vegetation stress across European biomes, notably in the context of drought detection.

1 | Introduction

PSII efficiency (ΦPSII) in photosynthetically active plants indicates a relative amount of absorbed photosynthetically active radiation that is used for photochemistry. It decreases under steady-state, light-exposed or stress conditions due to photoinhibiting adaptations, including solar-induced chlorophyll fluorescence (SIF) and a thermal dissipation called non-photochemical quenching (NPQ). Top-of-the-canopy (TOC) SIF is affected by both canopy structure and illumination conditions. Therefore, downscaling the canopy SIF and estimating the fluorescence quantum efficiency at the leaf level (ΦF), is essential for detecting physiological variations directly associated with plant photosynthetic activity (Dechant et al. 2020). This estimation relies on knowledge of the fluorescence escape probability (fesc), which quantifies the proportion of emitted SIF that escapes through the canopy, alongside the fraction of absorbed photosynthetically active radiation (fAPAR). Zeng

Dataset details:
Identifier: doi:10.26165/JUELICH-DATA/EFFTES
Creator: David Herrera
Dataset correspondence: d.herrera@fz-juelich.de
Title: Fluorescence Quantum Efficiency data for Europe 2018-2025
Publisher: Forschungszentrum Jülich GmbH
Publication year: 2025
(Resource type): Dataset
(Version): v1.0

et al. (2019) demonstrated that these two parameters can be approximated by the near-infrared reflectance of vegetation index (NIRv), defined as the product of the normalised difference vegetation index (NDVI) and near-infrared reflectance (Badgley et al. 2017). NIRv serves as a proxy for fAPAR and fesc and enables the downscaling of far-red fluorescence from the canopy to the leaf and even to the photosystem scales, given that fesc from the photosystem to the leaf scale approaches unity (Liu et al. 2019). The NIRv framework has been widely applied in studies aiming to estimate gross primary productivity (GPP) from satellite-derived SIF data (e.g., Zeng et al. (2019); Jiang et al. (2021)). Recent studies indicate that under environmental stress the relationship between canopy SIF and gross primary productivity can weaken or break down, as physiological regulation increasingly dominates the fluorescence signal. During extreme heat events, the linear SIF–GPP relationship has been shown to collapse, with non-photochemical quenching and other regulatory processes driving fluorescence dynamics independently of carbon uptake (Martini et al. 2022). Similarly, under chemical stress, physiological dynamics were found to dominate the response of canopy far-red SIF largely independent of canopy structure or absorbed radiation (Wu et al. 2022). More recent work further demonstrates that drought stress alters the coupling between SIF and GPP, highlighting limitations of canopy-scale SIF magnitude for stress detection (Pan et al. 2025). Together, these findings motivate the use of Φ*F*-type products to isolate physiological stress signals when conventional SIF–GPP relationships no longer hold.

To generate this dataset, we derive Φ*F* from currently available satellite observations using a multi-sensor formulation closely related to that proposed by Liu et al. (2023), but adapted to a different configuration and extended to daily temporal resolution for continental Europe, the UK and Ireland and northern Africa. The derivation of Φ*F* from multiple satellite sensors introduces uncertainty due to mismatches in overpass time and sun–sensor geometry between SIF and PAR observations, as discussed in Section 2.5. While alternative methods for estimating fesc, such as the fluorescence correction vegetation index (FCVI; Yang et al. (2020) and NIRv hyperspectral NIRvH and NIRvH2; Zeng et al. (2021)), have been proposed, they cannot be applied using TROPOMI data alone and require additional reflectance information from other satellite data. In the case of FCVI, this additional information comprises hyperspectral reflectance across multiple visible bands in addition to the near-infrared, whereas NIRvH and NIRvH2 rely on narrowband red and near-infrared reflectance bands. Recent studies have explored the possibility of obtaining the required visible-band reflectance information using RossThick-LiSparseR (RTLSR)-based Bidirectional Reflectance Distribution Function (BRDF) models (Zhang et al. 2023; Zhang and Zhang 2025). However, the reflectance information required to apply these models is not available in the TROPOMI data products used in this study, preventing their direct application.

2 | Data Description and Development

This dataset is based on spaceborne data from the ESA's Sentinel-5 Precursor (Sentinel-5P) satellite and NASA's Aqua and Terra satellites. The data span from May 2018 to August 2025, providing daily temporal resolution. Both datasets were resampled to a spatial resolution of 0.05° and were masked to exclude non-vegetated surfaces using the MODIS MCD12Q1 land cover classification (Friedl et al. 2002). To optimise processing efficiency, the majority of processing steps were carried out using Google Earth Engine (GEE) (Gorelick et al. 2017).

2.1 | Sentinel-5P—TROPOSIF Products

Sentinel-5P is a single-payload satellite equipped with the TROPOspheric Monitoring Instrument (TROPOMI), an imaging spectrometer designed for monitoring atmospheric trace gases and aerosols (Veefkind et al. 2012). Launched in October 2017, it has been providing data since May 2018. With a wide swath of 2600 km, the instrument enables near-daily global coverage at a maximum spatial resolution of 0.05°, centered around 13:30 local solar time (LST). Spectral Bands 5 and 6 cover the wavelength range from 665 to 785 nm, which is essential for retrieving SIF. Due to orbit overlap, multiple observations can occur within a single grid cell. To maintain consistency in the normalisation process and ensure uniform overpass timing across all pixels in a given orbit, only observations from the main orbit were used; thus, no averaging across overlapping observations was applied.

2.1.1 | SIF

The SIF data utilised in this study originate from the L2B SIF dataset (version 1.0.0), developed as part of the ESA TROPOSIF project (Guanter et al. 2021). SIF retrieval from TROPOMI is based on a data-driven method applied across two spectral windows (735–758 nm and 743–758 nm). The latter window is considered more robust and yields results comparable to the Caltech SIF product, which is also derived from TROPOMI data (Köhler, Frankenberg, et al. (2018); Guanter et al. (2021)). In addition to instantaneous SIF at 740 nm, the TROPOSIF dataset provides day-length-scaled SIF, which corrects for measurement time, sunrise and sunset, as well as the cosine of the solar zenith angle. This scaling enables better comparability with other SIF products recorded at different satellite overpass times and was added as an additional band to the dataset presented here (Guanter et al. 2021). For the calculation of Φ*F* in this dataset, instantaneous SIF was used to allow for temporal alignment with the PAR dataset. The original L2B data are provided in an ungridded format and were gridded daily to a maximum spatial resolution of 0.05°.

2.1.2 | NIRv

The TROPOSIF product also includes top-of-atmosphere reflectance measurements in the red, far-red and near-infrared (NIR) spectral regions with bands centered at 665, 680, 712, 741, 755, 773 and 781 nm, respectively. Following the approach of Guanter et al. (2021), the reflectance bands at 665 nm (red) and 781 nm (NIR) were used to compute the NIRv index, as described by Badgley et al. (2017).

$$\mathrm{NIRv} = \frac{\mathrm{NIR} - \mathrm{Red}}{\mathrm{NIR} + \mathrm{Red}} \times \mathrm{NIR} \quad (1)$$

While the reflectance data from TROPOMI are not corrected for directional effects or atmospheric influences, their key advantage lies in being acquired under the same sun-sensor geometry as the SIF observations. This consistency makes them preferable to using reflectance from other satellite sensors. Zeng et al. (2022) likewise recommend deriving NIRv from data collected by the same platform and under identical illumination conditions as the SIF measurements. As noted in Guanter et al. 2021, the specific spectral bands used were selected because of their relatively low sensitivity to atmospheric disturbances.

2.1.3 | Additional TROPOSIF Products

To account for the potential occurrence of hot-spot effects, an optical phenomenon that leads to angular anisotropy of SIF and subsequent artificially elevated SIF values observed by TROPOMI, the phase angle was calculated using the auxiliary data included in the TROPOSIF product (Guanter et al. (2021); Köhler, Guanter, et al. (2018)). The phase angle is defined as the angle between the sun and the sensor as viewed from the Earth's surface (Hapke 2012). Köhler, Guanter, et al. (2018) recommend filtering observations with phase angles between 20° and 60°. For Europe, these phase angles are between 20° in the lower and 80° in the higher latitudes. Data of Scandinavia should therefore be interpreted with caution as high phase angles can lead to artificially reduced SIF (Köhler, Guanter, et al. (2018)). Filtering by phase angle can be applied per use case as it has been added as an auxiliary band to the dataset.

To ensure data quality, observations with a cloud fraction greater than 20% were excluded using the cloud mask provided in the TROPOSIF dataset. This is consistent with the criteria used by Wang et al. (2020) and Zhang et al. (2019) and could still be tightened to below 20% if analysis should require it (the cloud fraction band is provided). It is worth noting that thin clouds have been shown to have minimal impact on SIF retrievals, so relaxing this threshold could be beneficial for future studies if data coverage becomes limiting (Frankenberg et al. (2012); Guanter et al. (2012)).

Finally, the top-of-atmosphere radiance data, which are also included in the TROPOSIF L2B product, were gridded for use in an alternative normalisation method (Dechant et al. (2022); De Cannière et al. (2024)). Allowing users to compare with the ΦF data calculated using PAR. This radiance band represents the total measured radiance within the SIF retrieval window (743–758 nm) and serves as a useful proxy for incoming PAR (Guanter et al. 2021).

2.2 | Aqua and Terra—MODIS Products

This dataset uses PAR data derived from the Moderate Resolution Imaging Spectroradiometer (MODIS). Specifically, the MCD18C2 and MCD18A2 products, which provide PAR estimates at 3-h intervals throughout the day, were employed. The MCD18C2 product is provided in geographic location at the target resolution of 0.05°, while the MCD18A2 uses a sinusoidal map projection at 1 km. PAR values are generated using a lookup table (LUT)-based retrieval method, which relies on MODIS top-of-atmosphere reflectance measurements (Wang 2024).

The data is provided globally in UTC; therefore, to match the overpass time of 13:30 LST, the LST at each UTC location was calculated using equation (2), where λ represents the longitude in degrees and 15 is the number of degrees Earth rotates per hour. PAR was then interpolated to match the LST using a linear interpolation between the two closest 3-h data points for each pixel.

$$\mathrm{UTC} = \mathrm{LST} - \frac{\lambda}{15} \tag{2}$$

In contrast to the narrow-band TOA radiance data of the TROPOSIF product, limited to the SIF retrieval window 743–758 nm, the MCD18C2 and MCD18A2 products provide a more complete estimate of total PAR, making them better suited for evaluating the light availability relevant to photosynthetic activity.

2.3 | Normalisation

To calculate ΦF, SIF was normalised for incoming radiation and canopy structure. Top-of-canopy (TOC) SIF can be described as follows (Guanter et al. 2014) (3):

$$\mathrm{SIF}_{\mathrm{canopy}} = \mathrm{PAR} \times \mathrm{fAPAR} \times \phi F \times f_{\mathrm{esc}} \tag{3}$$

Here, PAR refers to the incoming photosynthetically active radiation within the 400–700 nm range, while fAPAR denotes the fraction of PAR that is absorbed by the canopy. ΦF represents the fluorescence quantum efficiency at the leaf level, and fesc is the probability that a photon emitted as SIF at the leaf level escapes the canopy in sensor direction. Both fAPAR and fesc are affected by canopy structure. PAR and SIF describe the incoming radiation and the emitted fluorescence at the canopy scale, respectively. ΦF represents the fraction of absorbed PAR (APAR) that is re-emitted as fluorescence after correction for structural canopy effects. Variations in ΦF therefore reflect changes in the relative partitioning of absorbed energy among fluorescence, photochemical energy conversion and non-photochemical dissipation (e.g., heat), rather than serving as a direct measure of photosynthetic rate. As such, ΦF serves as a useful indicator of plant physiological status and provides insights into potential stress conditions (Liu et al. 2023). By rearranging Equation (3), ΦF can be calculated as follows:

$$\phi F = \frac{\mathrm{SIF}_{\mathrm{canopy}}}{\mathrm{PAR} \times \mathrm{fAPAR} \times f_{\mathrm{esc}}} \tag{4}$$

To estimate ΦF from daily satellite observations, the products of fesc for far-red SIF and fAPAR can be approximated using NIRv, as proposed by Zeng et al. (2019). In this dataset, ΦF was calculated using the instantaneous canopy SIF at 740 nm retrieved from TROPOMI at 13:30 LST, which was multiplied by π to approximate hemispherical SIF. This value was then combined with NIRv, derived from TROPOMI reflectance data and interpolated 13:30 LST PAR obtained from MODIS (see Section 2.2), as shown in Equation (5).

$$\phi F_{(\mathrm{NIRv})} = \frac{\pi \times \mathrm{SIF}^{740}_{\mathrm{canopy}}}{\mathrm{NIRv} \times \mathrm{PA}R} \quad (5)$$

The workflow to create the dataset is shown in Figure 1 with more detailed information on each band in Table 1 and quicklooks of all bands shown in Figure 2.

2.4 | Φ*F* Time Series of Plant Functional Types

To demonstrate the potential of the generated Φ*F* dataset, time series of Φ*F* and all variables involved in its calculation were analysed using plant functional types (PFTs) based on the classification by Harper et al. (2023). PFTs at the scale presented in this study have the benefit of having per pixel fractions of vegetation types and are widely used in the Earth System Modelling (ESM) community (Harper et al. 2023). The 2018 PFT classification was applied to all years, resampled to a spatial resolution of 0.05°. From the original eight PFT classes, two groups were created: croplands (including only 'GRASS-MAN' (managed grass), which in Harpers classification include all agricultural areas) and trees (including the PFTs: 'TREES-BD' (broad-leaved deciduous), 'TREES-BE' (broad-leaved evergreen), 'TREES-ND' (needle-leaved deciduous), 'TREES-NE' (needle-leaved evergreen)). The analysis was conducted for four countries, Spain, France, Germany and Poland, chosen for their extensive agricultural and forested areas. For each country, the median value of all available pixels was computed to illustrate the temporal trends of the different parameters throughout the vegetation periods. This approach was also applied to the decadal (Figures S1 and S2) and monthly data (Figures S3 and S4). Figures 3 and 4 present the vegetation period (March–October) across all years for the four countries and the four variables involved in the calculation of Φ*F*. Figure 4 shows variations in Φ*F* with notable outliers, especially in Germany and Poland, which are likely related to cloud cover, as evidenced by the corresponding drops in PAR.

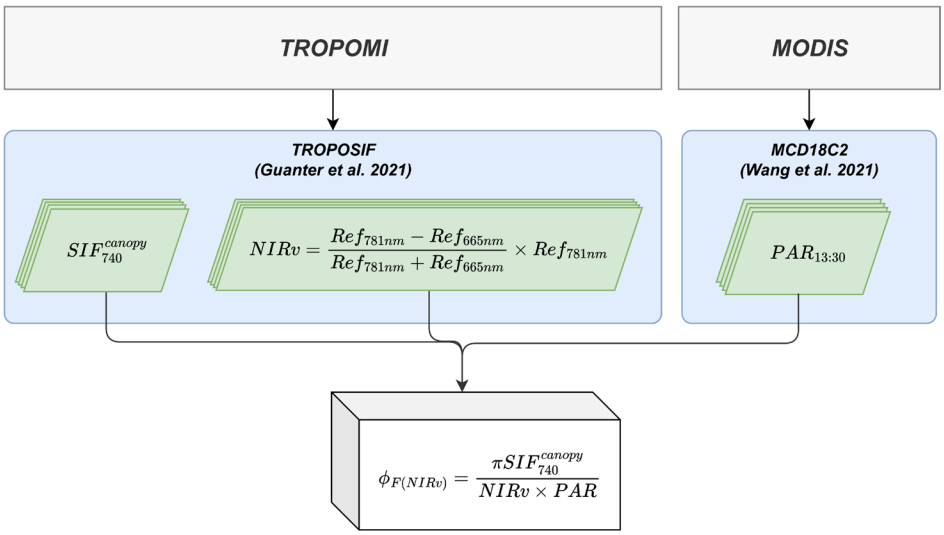

FIGURE 1 | Flowchart of the satellite products involved in calculating Φ*F*.

TABLE 1 | Bands included in the dataset with sources.

Band	Product	References	Unit
NIRv	Near-Infrared Reflectance of Vegetation	Badgley et al. (2017)	—
PAR	Photosynthetically Active Radiation at 13:30 LST	MODIS MCD18C2/MCD18A2 v0.62	mWm −2
Φ*F*	Fluorescence quantum efficiency at 740 nm	Adapted from Liu et al. (2023)	nm −1
SIF	Solar-Induced Fluorescence at 740 nm	Guanter et al. (2021)	mWm −2 sr −1 nm −1
SIF_dc	Solar-Induced Fluorescence daylength corrected	Guanter et al. (2021)	mWm −2 sr −1 nm −1
cloud_fraction	Cloud Fraction Cover	Guanter et al. (2021)	Percentage
phase_angle	Calculated from SZA, VZA and rel. Azimuth	Hapke (2012)	degree
sif_err	Solar-Induced Fluorescence Retrieval Error	Guanter et al. (2021)	mWm −2 sr −1 nm −1
toa_rad	Mean TOA Radiance in 743–758 nm fitting window	Guanter et al. (2021)	mWm− 2 sr −1 nm −1
SZA	Solar Zenith Angle	Guanter et al. (2021)	degree

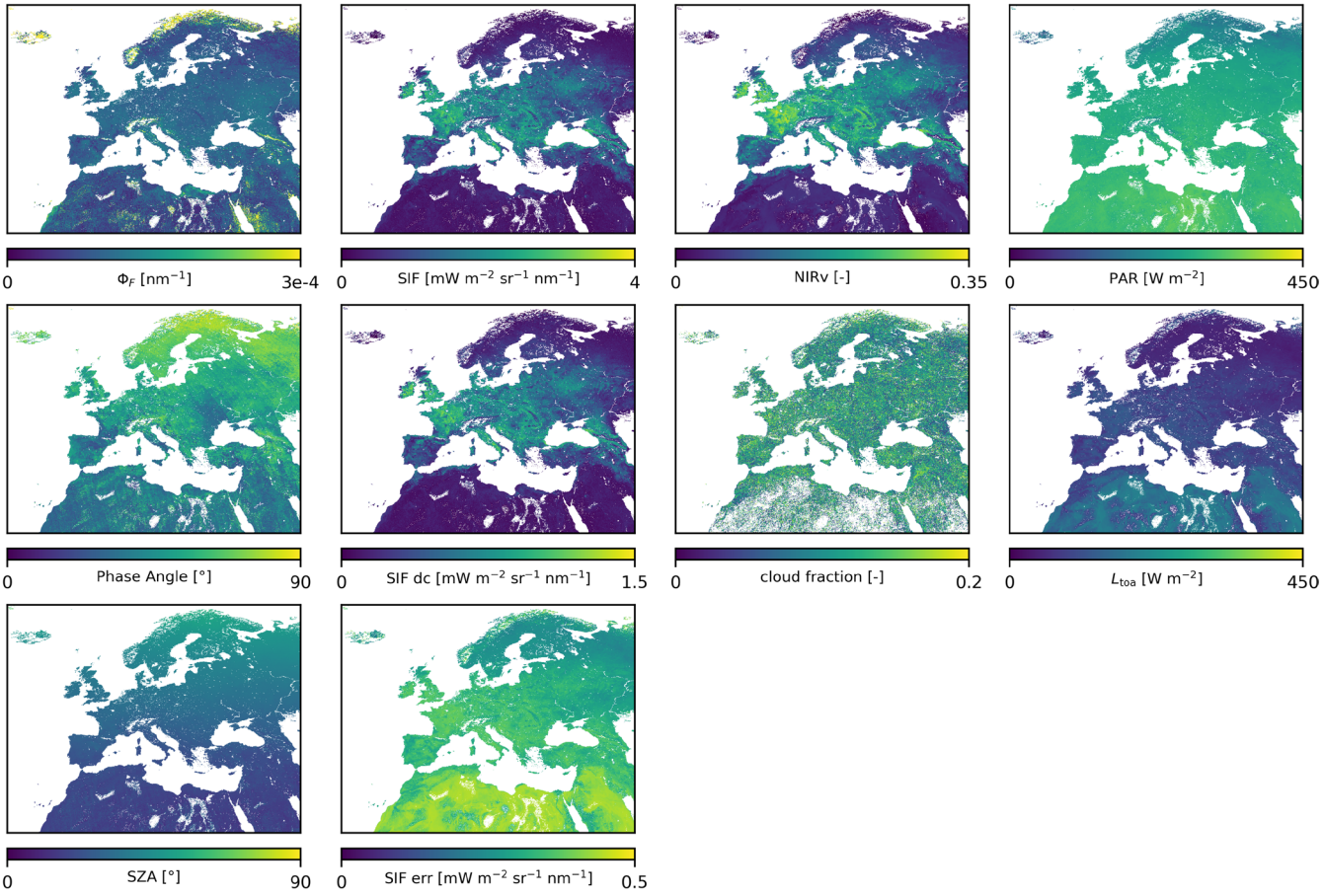

FIGURE 2 | Quicklooks of the layers included in the dataset. Median values per pixel from May 2018.

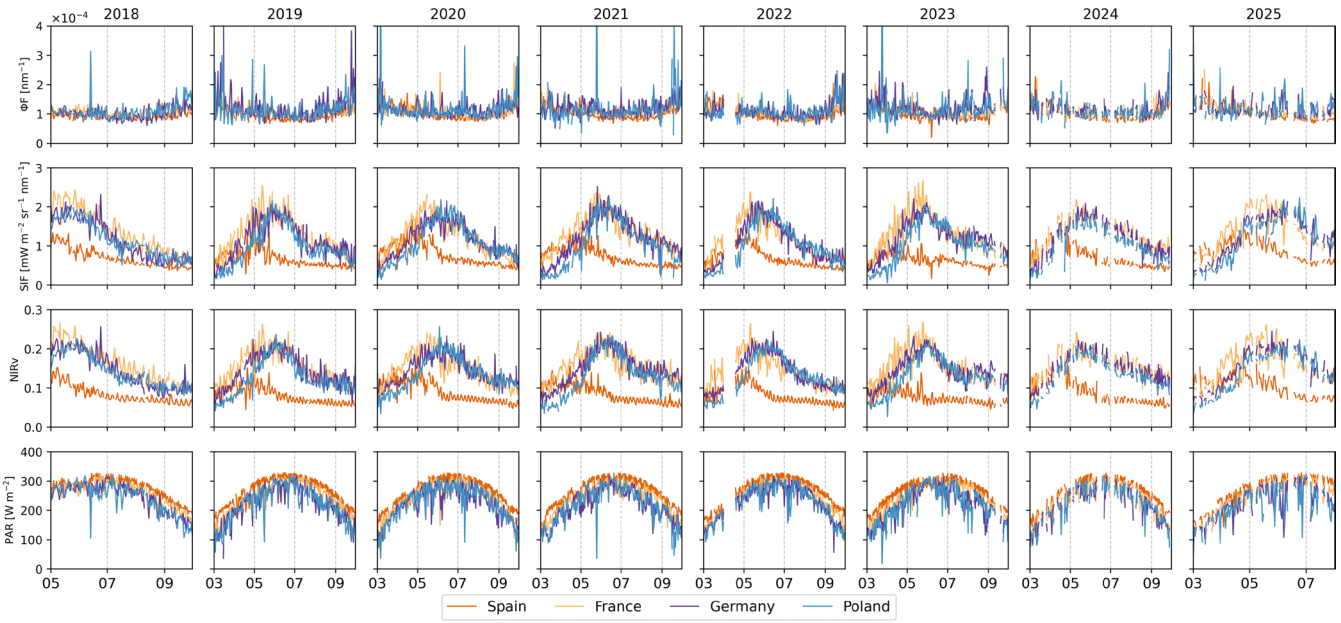

FIGURE 3 | Time series of vegetation periods from 2018 to 2025 for plant functional types classified as croplands. The plots display Φ*F* along with all contributing variables used in its calculation. Data cover the median of all available pixels in Spain, France, Germany and Poland.

For this purpose, the cloud fraction band is provided, allowing the filtering to be adjusted to thresholds lower than 20%. The seasonality visible in all four countries is completely removed, enabling change detection when compared with a reference dataset such as the soil moisture anomaly. This behaviour is illustrated in Figure 5, which is based on the median decadal time series averaged over all vegetation periods (March–October) for each country. Panel A shows the correlation of SIF and Φ*F* with

NIRv, together with their coefficients of variation (CV), for the agricultural PFT, while Panel B presents the same analysis for forests. For both vegetation classes, SIF exhibits a very high correlation with NIRv, reflecting the dominant influence of canopy structure and absorbed radiation on the top-of-canopy SIF signal. Although this relationship appears visually close to unity in Figure 5, the median decadal Pearson correlation coefficients remain consistently below 1 ($r \approx 0.96–0.99$ for agriculture and $r \approx 0.96–0.98$ for forests across countries), indicating residual variability not fully explained by canopy structure and absorbed radiation alone. This near-unity correlation should also be interpreted in the context of substantial spatial aggregation, as each decadal value represents the median across all available pixels within a country and PFT, thereby reducing local-scale heterogeneity and short-term variability. In contrast, two distinct patterns are evident for ΦF. First, the CV analysis shows a

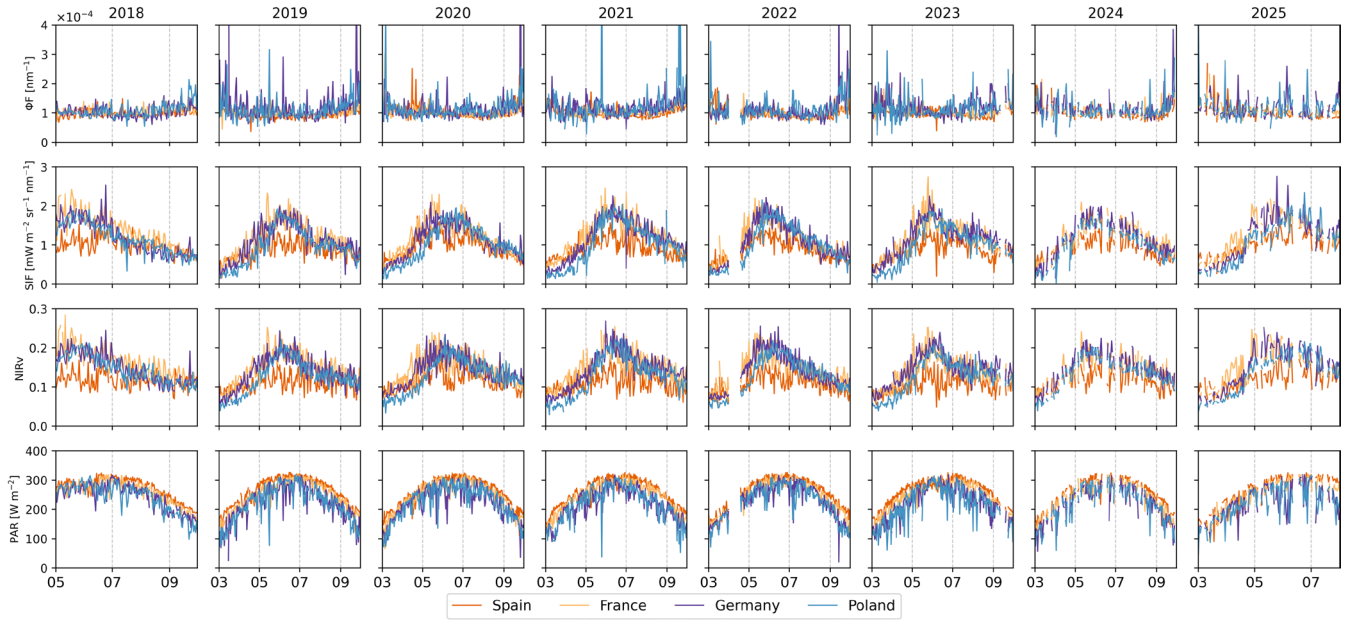

FIGURE 4 | Time series of vegetation periods from 2018 to 2025 for plant functional types classified as trees. The plots display ΦF along with all contributing variables used in its calculation. Data cover the median of all available pixels in Spain, France, Germany and Poland.

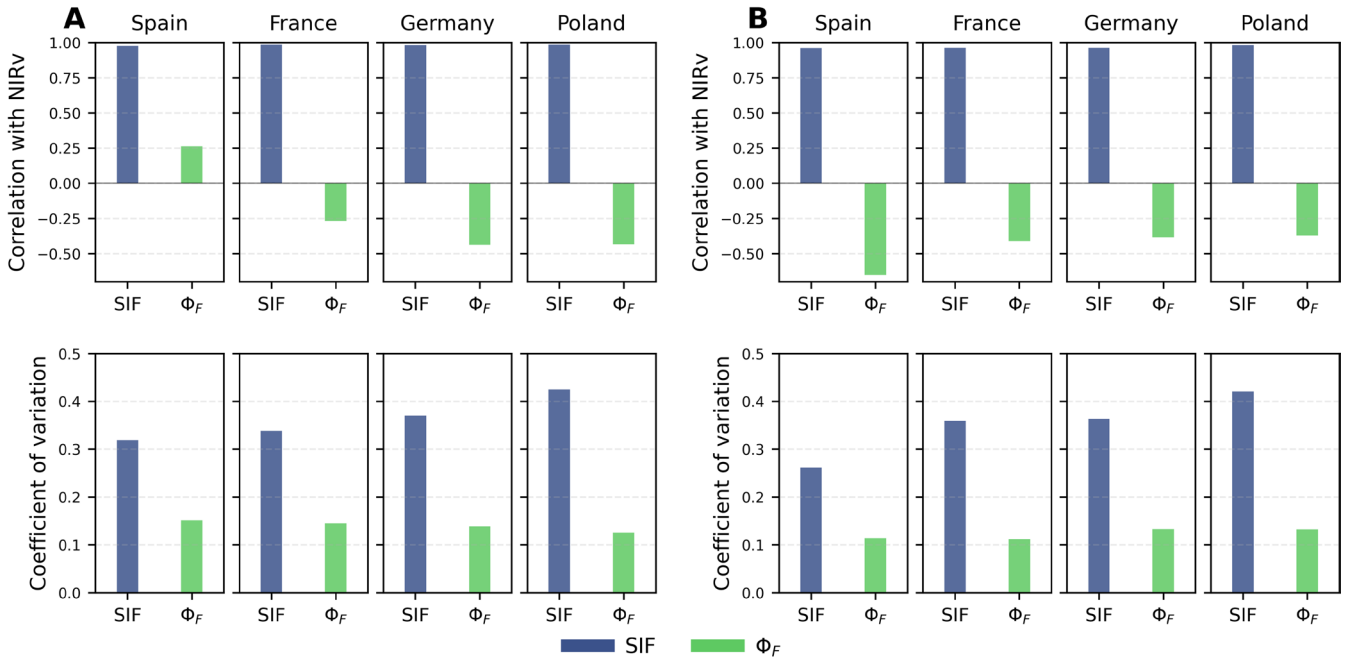

FIGURE 5 | Quantitative comparison between top-of-canopy SIF and ΦF using decadal time series. Panel A shows results for the forest plant functional type (PFT) and Panel B for the agricultural class. For each country, the upper row displays the Pearson correlation coefficient between NIRv and SIF (blue) and between NIRv and ΦF (green), while the lower row shows the corresponding coefficients of variation (CV). All metrics were computed using March–October data. Numerical values for monthly, decadal and daily aggregations are reported in Tables S1 and S2.

consistently reduced temporal variability of Φ*F* compared to SIF across all countries and vegetation classes, indicating a more temporally stable signal after normalisation. Second, the correlation between Φ*F* and NIRv is generally weak or inverse for most countries and PFTs, highlighting the effective decoupling of Φ*F* from canopy structure and absorbed radiation. Notable exceptions are observed for Spain, where positive ΦF–NIRv correlations emerge in the agricultural class and a comparatively strong correlation is also evident for forests, suggesting region-specific behaviour that warrants further investigation. Corresponding correlation and CV metrics at daily and monthly resolution are provided in (Tables S1 and S2).

2.5 | Limitations of Dataset

Optical data can only be recorded with minimal cloud cover. Which is the main limiting factor of this dataset. Figure 6, A depicts the percentage of observations below the 20% cloud cover threshold in the vegetation period of all years. Southern Europe, the Balkans and northern Africa show a much higher number of valid observations when compared to central and northern Europe. Analyses that rely on high temporal resolution are therefore more reliable in these areas. As the calculation of Φ*F* relies on clear-sky conditions, increasing cloud fraction corresponds to increasing uncertainty in Φ*F*. Another limiting factor in the higher latitudes is the phase angle (Figure 6B). Data that show a high phase angle should be interpreted with caution, as pointed out by Köhler, Guanter, et al. (2018). In their 2018 study, changes in the phase angle between 20° and 60° account for changes of up to 10% that are considered reasonable. Phase angles for Scandinavia and Scotland are within a range that accounts for higher variation and subsequently reduces the SIF signal. While the linear interpolation of PAR at 13:30 LST produces reasonable PAR throughout the entire area of interest, it is strongly simplified and will likely underestimate true PAR at 13:30 LST. It could potentially be replaced by a cosine function, though both methods should only be applicable in clear-sky conditions. In general, the error in PAR estimates is expected to be lowest when the three-hourly measurement times, 9:00, 12:00 and 15:00 UTC, are closest to the local UTC, as illustrated in Figure 6, C. Although PAR is interpolated to 13:30 LST on a per-pixel basis, thereby accounting for differences in illumination geometry, the underlying MODIS observations are acquired at an earlier time. As a result, inconsistencies in scene conditions, particularly due to transient cloud cover and associated shadows present at 10:30 LST but absent at 13:30 LST (or vice versa), may introduce residual uncertainties in the Φ*F* calculation. These residual uncertainties may introduce systematic latitudinal and seasonal effects. At higher latitudes and during periods with rapidly changing solar elevation, cloud dynamics and illumination conditions tend to vary more strongly within the morning–early afternoon time window, increasing the likelihood of scene inconsistencies between PAR and SIF observations. In contrast, lower latitudes and summer months are characterised by more stable midday illumination and cloud conditions, reducing the impact of this mismatch. While strict cloud filtering and spatial aggregation mitigate these effects, they should be considered when interpreting regional and seasonal patterns in Φ*F*. In general, tightening the cloud fraction mask is

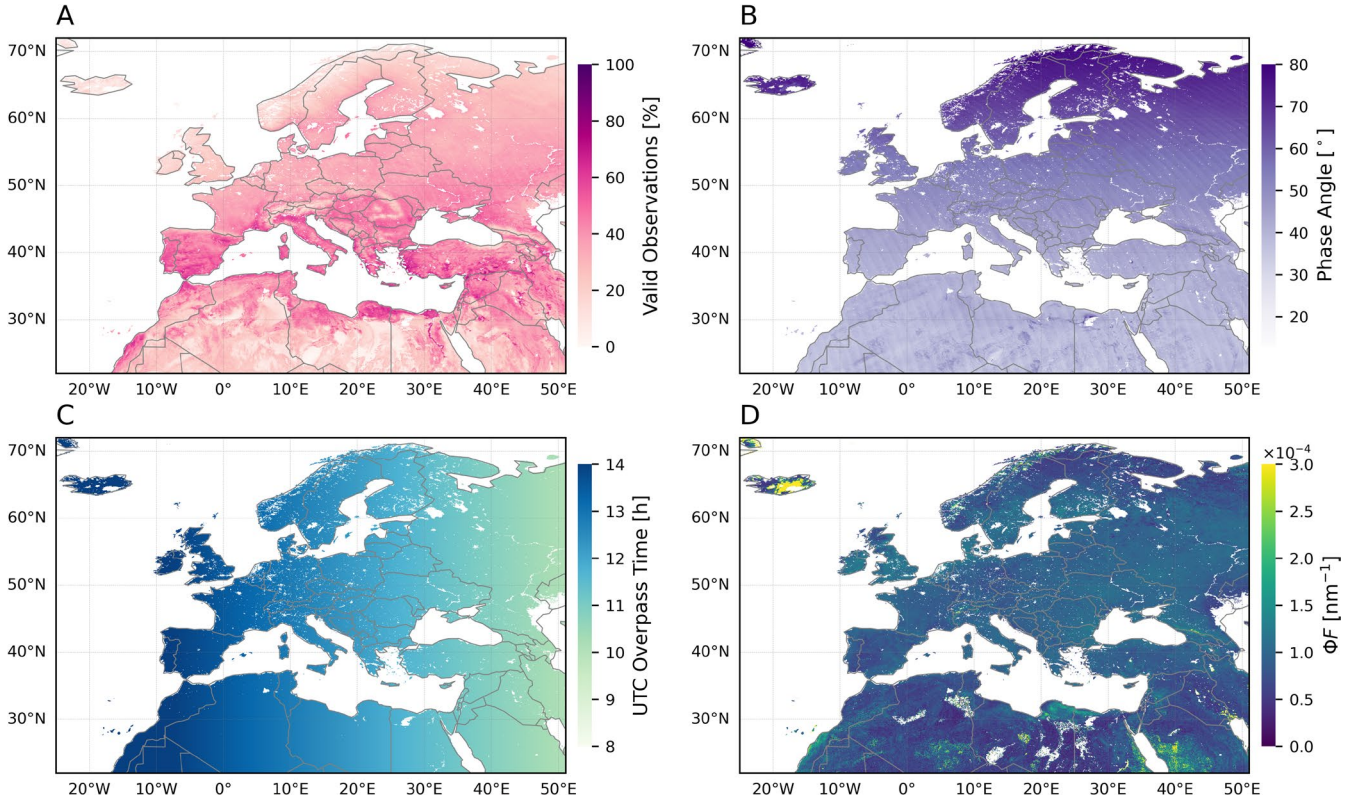

FIGURE 6 | Maps illustrating quality indicators for the generated European dataset. Panel (A) displays the percentage of valid observations for all vegetation periods (March–October). Panel (B) presents the average phase angle for each location across the full dataset. Panel (C) shows the variation in UTC overpass times relative to 13:30 LST. Panel (D) depicts the spatial distribution of Φ*F*, averaged over the first 2 weeks of June 2019.

expected to improve the accuracy of the dataset, but it would reduce the number of observations. The Φ*F* dataset still lacks validation, which will likely only be possible after the launch of the Fluorescence Explorer (FLEX) in 2026 (ESA 2025). FLEX will provide a fluorescence quantum efficiency product, which could be used for comparison. Although the intercomparison of satellite SIF products led to good results (Guanter et al. (2021), Köhler, Frankenberg, et al. (2018)), direct validation with in situ measurements at 0.05° remains challenging (Du et al. 2023). In this context, the 300 m ground sampling distance of FLEX will aid in validating SIF-derived higher-level products, including Φ*F*. SIF-derived higher-level products, including Φ*F*.

3 | Dataset Access

The dataset is accessible through the Jülich Data Platform in netcdf format. The three temporal resolutions (daily, decadal and monthly) are made available as separate files. The data structure is the same with the exception that the decadal and monthly data are provided with a start and end date for the temporal averaging. The data structure follows the HARP principles for intercomparison between remote sensing datasets.

4 | Potential Dataset Use and Reuse

A subset of this dataset was used in a previous scientific study (Herrera et al., under review). We combined the Φ*F* data with a subsurface water storage anomaly product over six vegetation periods to identify a lagged response of Φ*F* to agricultural drought in Germany. The observed two-day lag in both agricultural areas and forests was also evident in Land Surface Temperature data, highlighting the potential of our approach to normalise SIF by calculating Φ*F* to detect actual physiological changes in plants. The spatial extend of the presented dataset matches the Combined Drought Indicator (CDI) data provided by the European Drought Observatory (EDO) and could therefore be tested as a potential extension to the current monitoring scheme (European Commission, Joint Research Centre (JRC) 2022). The quick reaction of Φ*F* to agricultural drought has the potential to increase the timeliness of drought detection at the European level. While drought detection was the primary motivation for developing this dataset, the direct relationship between Φ*F* and photosynthetic activity allows for broader applications in monitoring vegetation stress. In this context, Φ*F* is best suited for analysing relative changes, anomalies and temporal dynamics of vegetation stress, whereas it should not be interpreted as an absolute measure of photosynthetic efficiency or carbon assimilation. Given the diversity of ecosystems across Europe and northern Africa, the dataset can support sensitivity analyses to determine under which conditions a clear link between Φ*F* and certain stress factors can be observed, and when such connections may weaken or disappear. The high temporal resolution of the presented dataset with daily, decadal and monthly intervals is a key advantage, enabling the dataset to be used for detecting both short-term fluctuations and long-term trends in Φ*F*. Moreover, all variables used to compute Φ*F* are provided in this dataset, allowing the creation of alternative products, such as a normalised Φ*F* dataset that includes day-length correction, tailored to specific research needs.

5 | Conclusions

The presented dataset is intended to support the development of other vegetation stress products that would go beyond drought stress. The daily, decadal and monthly temporal resolution of the presented dataset enables the analysis of both short- and long-term responses of Φ*F* that can be compared to other relevant vegetation properties. Since Φ*F* is directly related to changes in photosynthetic activity of plants, it does not rely on anomaly calculations to detect temporal changes. The calculation of the presented Φ*F* product was performed using high-quality satellite products provided by ESA and NASA. However, the MODIS PAR product used to calculate Φ*F* differs from the TROPOSIF product in sun–sensor geometry. Despite this discrepancy, the results produced from a subset of the data used by Herrera et al. (unpublished) indicate that the generated Φ*F* dataset effectively captures the physiological component of the top-of-the-canopy SIF signal.

Acknowledgements

This work has partially been funded by the Deutsche Forschungsgemeinschaft (DFG, German Research Foundation) under Germany's Excellence Strategy—EXC 2070-390732324 and the Federal German Ministry for Economic Affairs and Climate Action (BMWK) within the DroughtMAP project under the grant number 50EE2233. Open Access was funded by the Deutsche Forschungsgemeinschaft (DFG, German Research Foundation)—491111487. Open Access funding enabled and organized by Projekt DEAL.

Funding

BMWK, Grant/Award Number: 50EE2233.

Conflicts of Interest

The authors declare no conflicts of interest.

Data Availability Statement

The data that support the findings of this study are openly available in www.data.fz-juelich.de at https://data.fz-juelich.de/dataset.xhtml?persistentId=doi:10.26165/JUELICH-DATA/EFFTES, reference number doi: 10.26165/JUELICH-DATA/EFFTES.

References

Badgley, G., C. B. Field, and J. A. Berry. 2017. "Canopy Near-Infrared Reflectance and Terrestrial Photosynthesis." *Science Advances* 3, no. 3: e1602244.

De Cannière, S., M. Baur, D. Chaparro, T. Jagdhuber, and F. Jonard. 2024. "Water Availability and Atmospheric Dryness Controls on Spaceborne Sun-Induced Chlorophyll Fluorescence Yield." *Remote Sensing of Environment* 301: 113922.

Dechant, B., Y. Ryu, G. Badgley, et al. 2020. "Canopy Structure Explains the Relationship Between Photosynthesis and Sun-Induced Chlorophyll Fluorescence in Crops." *Remote Sensing of Environment* 241: 111733.

Dechant, B., Y. Ryu, G. Badgley, et al. 2022. "NIRVP: A Robust Structural Proxy for Sun-Induced Chlorophyll Fluorescence and Photosynthesis Across Scales." *Remote Sensing of Environment* 268: 112763.

Du, S., X. Liu, J. Chen, W. Duan, and L. Liu. 2023. "Addressing Validation Challenges for TROPOMI Solar-Induced Chlorophyll Fluorescence

Products Using Tower-Based Measurements and an NIRv-Scaled Approach'." *Remote Sensing of Environment* 290: 113547.

European Commission, Joint Research Centre (JRC). 2022. EDO Combined Drought Indicator (CDI) (version 4.0.0).

European Space Agency (ESA). 2025. "Announcement of opportunity for FLEX cal/val." Earth Online. https://earth.esa.int/eogateway/announcement-of-opportunity/flex-cal-val.

Frankenberg, C., C. O'Dell, L. Guanter, and J. McDuffie. 2012. "Remote Sensing of Near-Infrared Chlorophyll Fluorescence From Space in Scattering Atmospheres: Implications for Its Retrieval and Interferences With Atmospheric CO_2 Retrievals." *Atmospheric Measurement Techniques* 5, no. 8: 2081–2094.

Friedl, M. A., D. K. McIver, J. C. F. Hodges, et al. 2002. "Global Land Cover Mapping From MODIS: Algorithms and Early Results." *Remote Sensing of Environment* 83, no. 1: 287–302.

Gorelick, N., M. Hancher, M. Dixon, S. Ilyushchenko, D. Thau, and R. Moore. 2017. "Google Earth Engine: Planetary-Scale Geospatial Analysis for Everyone." *Remote Sensing of Environment* 202: 18–27.

Guanter, L., C. Bacour, A. Schneider, et al. 2021. "The TROPOSIF Global Sun-Induced Fluorescence Dataset From the Sentinel-5P TROPOMI Mission." *Earth System Science Data* 13, no. 11: 5423–5440.

Guanter, L., C. Frankenberg, A. Dudhia, et al. 2012. "Retrieval and Global Assessment of Terrestrial Chlorophyll Fluorescence From GOSAT Space Measurements." *Remote Sensing of Environment* 121: 236–251.

Guanter, L., Y. Zhang, M. Jung, et al. 2014. "Global and Time-Resolved Monitoring of Crop Photosynthesis With Chlorophyll Fluorescence." *Proceedings of the National Academy of Sciences* 111, no. 1: E1327–E1333.

Hapke, B. 2012. *Theory of Reflectance and Emittance Spectroscopy*. Cambridge University Press.

Harper, K. L., C. Lamarche, A. Hartley, et al. 2023. "A 29-Year Time Series of Annual 300 m Resolution Plant-Functional-Type Maps for Climate Models." *Earth System Science Data* 15, no. 3: 1465–1499.

Jiang, C., K. Guan, G. Wu, B. Peng, and S. Wang. 2021. "A Daily, 250m and Real-Time Gross Primary Productivity Product (2000–Present) Covering the Contiguous United States." *Earth System Science Data* 13, no. 2: 281–298.

Köhler, P., C. Frankenberg, T. S. Magney, L. Guanter, J. Joiner, and J. Landgraf. 2018. "Global Retrievals of Solar-Induced Chlorophyll Fluorescence With TROPOMI: First Results and Intersensor Comparison to OCO-2." *Geophysical Research Letters* 45, no. 19: 10456–10463.

Köhler, P., L. Guanter, H. Kobayashi, S. Walther, and W. Yang. 2018. "Assessing the Potential of Sun-Induced Fluorescence and the Canopy Scattering Coefficient to Track Large-Scale Vegetation Dynamics in Amazon Forests." *Remote Sensing of Environment* 204: 769–785.

Liu, X., L. Guanter, L. Liu, et al. 2019. "Downscaling of Solar-Induced Chlorophyll Fluorescence From Canopy Level to Photosystem Level Using a Random Forest Model." *Remote Sensing of Environment* 231: 110772. https://doi.org/10.1016/j.rse.2018.05.035.

Liu, X., L. Liu, C. Bacour, et al. 2023. "A Simple Approach to Enhance the TROPOMI Solar-Induced Chlorophyll Fluorescence Product by Combining With Canopy Reflected Radiation at Near-Infrared Band." *Remote Sensing of Environment* 284: 113341.

Martini, D., K. Sakowska, G. Wohlfahrt, et al. 2022. "Heatwave Breaks Down the Linearity Between Sun-Induced Fluorescence and Gross Primary Production." *New Phytologist* 233, no. 6: 2415–2428. https://doi.org/10.1111/nph.17920.

Pan, Q., C. He, S. Sun, et al. 2025. "Effects of Drought Stress on the Relationship Between Solar-Induced Chlorophyll Fluorescence and Gross Primary Productivity in a Chinese Cork Oak Plantation." *Remote Sensing* 17, no. 12: 2017. https://doi.org/10.3390/rs17122017.

Veefkind, J. P., I. Aben, K. McMullan, et al. 2012. "TROPOMI on the ESA Sentinel-5 Precursor: A GMES Mission for Global Observations of the Atmospheric Composition for Climate, Air Quality and Ozone Layer Applications." *Remote Sensing of Environment* 120: 70–83.

Wang, C., K. Guan, B. Peng, et al. 2020. "Satellite Footprint Data From OCO-2 and TROPOMI Reveal Significant Spatio-Temporal and Inter-Vegetation Type Variabilities of Solar-Induced Fluorescence Yield in the U.S. Midwest." *Remote Sensing of Environment* 241: 111728.

Wang, D. 2024. 'MODIS/Terra+Aqua Photosynthetically Active Radiation Daily/3-Hour L3 Global 0.05Deg CMG V062|NASA Earthdata'.

Wu, G., K. Guan, C. Jiang, et al. 2022. "Attributing Differences of Solar-Induced Chlorophyll Fluorescence (SIF)-Gross Primary Production (GPP) Relationships Between Two C4 Crops: Corn and Miscanthus." *Agricultural and Forest Meteorology* 323: 109046. https://doi.org/10.1016/j.agrformet.2022.109046.

Yang, P., C. van der Tol, P. K. E. Campbell, and E. M. Middleton. 2020. "Fluorescence Correction Vegetation Index (FCVI): A Physically Based Reflectance Index to Separate Physiological and Non-Physiological Information in Far-Red Sun-Induced Chlorophyll Fluorescence." *Remote Sensing of Environment* 240: 111676.

Zeng, Y., G. Badgley, B. Dechant, Y. Ryu, M. Chen, and J. A. Berry. 2019. "A Practical Approach for Estimating the Escape Ratio of Near-Infrared Solar-Induced Chlorophyll Fluorescence." *Remote Sensing of Environment* 232: 111209.

Zeng, Y., D. Hao, G. Badgley, et al. 2021. "Estimating Near-Infrared Reflectance of Vegetation From Hyperspectral Data." *Remote Sensing of Environment* 267: 112723.

Zeng, Y., D. Hao, A. Huete, et al. 2022. "Optical Vegetation Indices for Monitoring Terrestrial Ecosystems Globally." *Nature Reviews Earth & Environment* 3, no. 7: 477–493.

Zhang, Z., J. Chen, L. Guanter, L. He, and Y. Zhang. 2019. "From Canopy-Leaving to Total Canopy Far-Red Fluorescence Emission for Remote Sensing of Photosynthesis: First Results From TROPOMI." *Geophysical Research Letter* 46, no. 21: 12030–12040. https://doi.org/10.1029/2019GL084832.

Zhang, Z., and Y. Zhang. 2025. "Fluorescence Efficiency-Derived Physiological Optimal Temperature Improving the Estimation of Photosynthesis." *Geophysical Research Letters* 52, no. 15: e2025GL116420. https://doi.org/10.1029/2025GL116420.

Zhang, Z., Y. Zhang, and Y. Zhang. 2023. "Generating High-Resolution Total Canopy SIF Emission From TROPOMI Data: Algorithm and Application." *Remote Sensing of Environment* 295: 113699. https://doi.org/10.1016/j.rse.2023.113699.

Supporting Information

Additional supporting information can be found online in the Supporting Information section. **Data S1:** Supporting Information.